Thermodynamic analysis in laminar falling film evaporator

Arnat Mahamoudou, Julien Ramousse, Nicolas Cellier, Nolwenn Le Pierrès

Thermodynamic analysis in laminar falling film evaporator

Arnat Mahamoudou [a], Julien Ramousse [a,*], Nicolas Cellier [a,b], Nolwenn Le Pierrès [a]

[a] Laboratoire LOCIE, CNRS UMR5271 – Université Savoie Mont-Blanc, 73370 Le Bourget-du-Lac, France
[b] CGI, IMT Mines Albi, 81000 Albi, France

A B S T R A C T

An evaporative laminar falling film flowing by gravity on a vertical plate heated by a heat transfer fluid is studied to determine the local temperature, entropy generation and evaporated mass flow, assuming constant saturation pressure at the free interface, in co-current and counter-current configurations. The heat transfer fluid and film energy equations are solved simultaneously through a 2D model using an implicit finite difference scheme. Local and global analysis were performed in order to study the impact of parameters such as the heat transfer fluid and film Reynolds numbers and inlet film temperature on entropy generation (thermal and viscous irreversibilities) and on thermal and evaporation efficiencies. Results show that the increase of the overall thermal entropy generation leads to the increase of the evaporated mass flow rate. Both increase with the increase of the heat transfer fluid Reynolds number and decreases with the increase of the film Reynolds number for both configurations. The inlet film temperature – overheated or subcooled inlet fluid flow - also impacts the evaporation process. The influence of the Reynolds number and temperature difference on the heat transfer coefficients of both fluids and for both configurations is also discussed.

1. Context and state of the art

A heat exchanger is usually a device that allows to transfer heat from a fluid to another one. These fluids could be liquid, gas or a combination of both. It is a common unit used in many engineering applications such as air conditioning, refrigeration, heating and so on. Thin falling film heat exchangers are a type of heat exchanger that have the advantage of intensifying heat exchange by offering great exchange surface, high transfer coefficients and working with small temperature gradients [1]. They can be found in a number of important technical applications such as condensers [2], evaporators [3] or absorption systems [4,5]. Falling film evaporators are phase-change heat exchangers that involve falling film evaporating on its free surface. They are used mostly in conjunction with other equipments and thus have a significant impact on the system efficiency. Therefore, the study and understanding of the phenomena encountered on these types of evaporators at component scale (1D model), have been until now important [6–8]. More recently, researchers have gone further by analyzing more deeply local phenomena (2 and 3D models) with the aim of understanding how local parameters can influence the component efficiency [9,10].

The first local analysis made on falling film was carried out by Nusselt [11] by determining the theoretical stream-wise velocity profile of a falling liquid film. Afterwards, a significant amount of analytical, numerical and experimental researches on falling film heat, mass and hydrodynamic phenomena has been conducted. Critical reviews of these different phenomena in falling films were carried out by Killion and Garimella [12] and Mahamoudou et al. [13]. Although, the experimental study conducted by Karimi and Kawaji [14] on falling film showed a significant difference between their result and the Nusselt's predictions in a wavy turbulent films, the experimental analyses carried out by Ambrosini et al. [15] on a water film falling down a flat plate at different inclinations and temperature (between 20–30 °C and 50–70 °C for cold and warm water films respectively) showed that the Nusselt theory represents at low Reynolds numbers the falling film velocity.

Many authors studied the parameters that impact the falling film exchanger performance such as the fraction of effective evaporation area and the amount of evaporation rate. Ben Jabrallah et al. [16] studied, through a numerical and experimental study, the evaporation of a falling film that flows down on a vertical plate heated by a constant heat flux. The vapor produced is condensed on the opposite wall maintained at constant and uniform temperature. The transfer phenomena in the gas phase were considered in their equations. They found that the thermodynamic state of the liquid film is impacted by the heat flux and the temperature of the condensation wall but also by the water feed temperature and flow rate of the film. In general, the operating conditions

* Corresponding author.
E-mail address: julien.ramousse@univ-smb.fr (J. Ramousse).

Nomenclature

A	Surface, (m^2)
C_p	Thermal capacity, $\left(J.K^{-1}.kg^{-1}\right)$
e	Thickness, (m)
g	Gravitational acceleration, $(m.s^{-2})$
h	Global heat transfer coefficient, $\left(W.m^{-1}.K^{-1}\right)$
$\Delta H_{liq-vap}$	Latent heat of evaporation of the film fluid, $\left(J.kg^{-1}\right)$
L	Evaporator length, (m)
l	Evaporator width, (m)
$\dot{m}$	Flow rate, $\left(kg.s^{-1}\right)$
$\dot{q}$	Surface heat flux, $\left(W.m^{-2}\right)$
$\dot{Q}$	Heat exchanger power,(W)
R	Capacity flow rates ratio, $(-)$
Re	Reynolds number, $(-)$
$\dot{S}_{gen}$	Entropy generation rate , $\left(W.K^{-1}\right)$
T	Temperature, (K)
u	Flow velocity, $\left(m.s^{-1}\right)$
$\bar{u}$	Mean velocity, $\left(m.s^{-1}\right)$

Greek symbols

Γ	Mass flow rate per unit of width, $\left(kg.s^{-1}.m^{-1}\right)$
δ	Boundary layer, (m)
ε	Efficiency, $(-)$
λ	Conductivity, $\left(W.K^{-1}.m^{-1}\right)$
μ	Dynamic viscosity, (Pa.s)
ρ	Density, $\left(kg.m^{-3}\right)$
$\dot{\sigma}$	Volumic entropy generation rate, $\left(W.K^{-1}.m^{-3}\right)$
τ_{evap}	Evaporation rate, $(-)$
$\bar{\bar{\tau}}$	Shear stress tensor, (Pa)

Subscripts

bulk	Bulk
evap	Evaporated
fluid	Heat transfer fluid or falling film
gen	Generated
htf	Heat transfer fluid
f	Film
in	Inlet
interface	Liquid − vapor interface
max	Maximum
out	Outlet
sat	Saturated
th	Thermal
v	Viscous
w	Wall

surely impact the transfers but the design of the evaporator must also be done carefully as its impact is also considerable [6]. The latter showed that in addition to the previously mentioned parameters, the overall heat transfer is also impacted by the evaporating temperature, the liquid density and the viscosity and the tube diameter. By performing an experimental study on a vertical falling film, Prost et al. [17] obtained a general correlation for the calculation of the film heat transfer as a function of the film Reynolds and Prandtl numbers. An experimental investigation of the heat transfer characteristics of the falling film evaporation of Freon HCFC 123 in a plate-fin heat exchanger was carried out by Zhou et al. [18] and showed that the local heat transfer coefficient varies with the inlet mass flow rate and the heat flux at the wall. These few different references mentioned above summarize the variables that must be controlled to evaluate the falling film in a general manner. Krupiczka et al. [19] explained through an experimental study, that in practice the evaporation rate is small compared to the inlet film flow and so the film thickness and the heat transfer coefficient are practically constant in the fully developed flow regime. In their work, they studied the case of a water, methanol and isopropanol falling film and maintained the film at a temperature close to the saturation conditions.

Although many authors apply the second law of thermodynamics at the component scale to improve and optimize the exchanger performance, more recently, searchers started to apply the Thermodynamic of Irreversible Process (TIP) at local scale, to identify the sources of entropy generation to enable a deeper assessment of the falling film exchanger performance. An investigation of the entropy generation of a fully developed laminar falling liquid film that flows down an inclined heated plate while the upper surface is free and adiabatic was developed by different authors [20–22] without considering the evaporation phenomenon. They highlighted that the entropy generation is due to the thermal and viscous entropy generations, and concluded that the fluid friction irreversibilities are impacted by the type of fluid: physical properties and Newtonian or non-Newtonian fluid assumption, while the thermal irreversibilities are mainly caused by the heat transfer. Therefore, it is of practically significance to develop a simple, but accurate and reliable model to control the parameters that have direct impact on the operation of the evaporators and consequently on the generated entropy.

In this paper, the focus is on the study of vertical plate falling film evaporator. This type of evaporator can be found on absorption machines and are mainly used for small-capacity machines as they are more compact and cheaper compared to tubular heat exchangers [23,24]. Three novelties have to be underlined in this work. The first one is the study of the falling film by describing the heat coupling between the heat transfer fluid (HTF) and the film through the wall and simultaneously solving the energy equations in both fluids considering a 2D-model. Indeed, the HTF is modelled considering the 2D heat transfer equation instead of just calculating an overall heat transfer coefficient or assuming extreme cases, and thus allowing to model more realistic cases. The second novelty of this paper is the local analysis of the entropy generation through the whole falling film evaporator – considering not only the film but also the HTF and the wall in order to quantify the part of irreversibilities generated in each medium as a function of the operating conditions. Most of the authors applied the local analysis of the second law of thermodynamics only on the film. The third point that has to be underlined here is the link made between the local entropy generation and the overall exchanger one. The objective is to analyze the evaporation process, and to understand the impact of the thermal and hydrodynamic phenomena on the entropy generation. In the following sections, the problem is formulated, analyzed, solved and discussed. Based on the phenomena modelling in the HTF and falling film, the effect of film overheating and subcooling as well as the HTF and film Reynolds number, considering laminar flow regime, on the evaporation rate and on the entropy generation is studied. Other parameter impact such as the evaporator length is also analyzed and results are given at both local and component scales. The study is done for both co and counter-current configurations for comparison. This study is of a great of interest as it can be used as a tool to minimize entropy generation for heat exchangers' design and optimization. It is a tool for the design of falling film evaporators, for cooling and heating absorption machines, based on an entropy generation analysis by understanding how different parameters impact both irreversibility and performance.

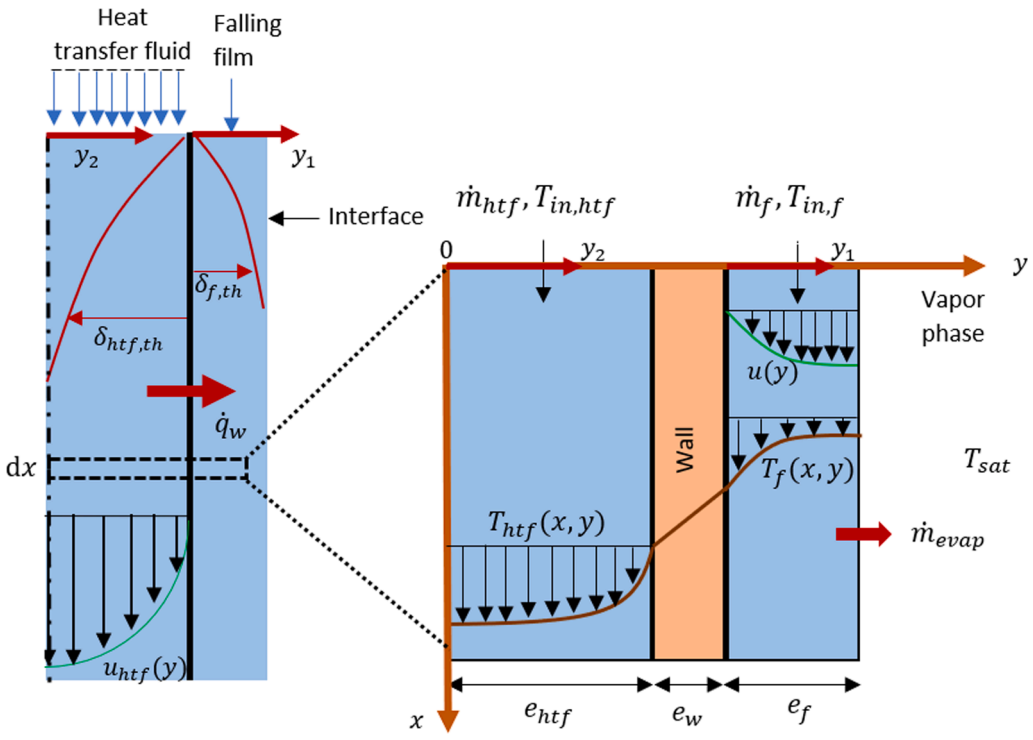

Fig. 1. Description of a vertical falling film evaporator at local scale.

2. Problem description

2.1. Studied configuration

The study and analysis of the entropy generation produced during the evaporation process requires an understanding of the heat and viscous phenomena encountered. Fig. 1 shows a laminar film of incompressible liquid that enters the evaporator component at $x = 0$. The film flows down under the gravity effect (from the top to the bottom) over a vertical plate heated by means of a HTF. The latter can be in co–current (from the top to the bottom) or counter–current (from the bottom to the top) with the falling film. The HTF enables to increase the film temperature and then to evaporate a part of it at the free interface, assumed at constant saturation temperature along the film (constant pressure).

The heat and viscous transfer phenomena lead to the formation of the thermal δ_{th} boundary layer in the HTF ($\delta_{htf,th}$) and in the film ($\delta_{f,th}$). From Fig. 1, $x = 0$ and $x = L$ at the input and output of the absorber respectively while the axis y is equal to zero at the center of the HTF channel and to $e_{htf} + e_w + e_f$ at the falling film interface. The axis $y_1 \in [0, e_f]$, it varies from the heated plate – film side – until the film interface while the axis $y_2 \in [0, e_{htf}]$, it varies from the center of the HTF channel thickness to the heated plate – HTF side.

2.2. Model description

2.2.1. Model assumptions

Heat transfer is greatly intensified in the presence of capillary and solitary waves in the film [25]. However, this paper will be limited to the modeling of falling film in the established laminar regime where these wave phenomena are attenuated [26] as the falling film Reynolds number is considered to be lower or equal to 200. Moreover, as the impact of edge effect in this falling film is almost non-existent and as the vertical plate is assumed to be smooth and without corrugation, a 2D model seems to be appropriate to model the problem. However, for heat transfer fluids flowing over ribbed or corrugated plates, it is strongly advised to take into account the impact of edge effects by using 3D models. In formulating this model, the following assumptions were made:

- The falling film flow is assumed to be laminar, one-dimensional and fully developed hydrodynamically throughout.
- The liquid solution is incompressible, Newtonian and its physical properties (the viscosity, thermal conductivity and specific heat) are assumed constant since the flow is in steady-state and the temperature difference between the evaporator inlet and outlet is small – about 5 °C.
- The evaporated mass is negligible compared to the inlet mass flow rate of the film ($\dot{m}_{evap} \ll \dot{m}_f$). Indeed, the film thickness is assumed to be small compared to the length of the evaporator and the interfacial shears are negligible. Consequently, the mass flow rate of the film $\dot{m}_f$ is assumed constant so as its thickness e_f along x.
- The evaporation process occurs at constant pressure, so that the saturation temperature T_{sat} at the interface is constant along x.
- There are no shear forces exerted on the film by the vapor at the interface.

2.2.2. Hydraulic model

2.2.2.1. Falling film. As the falling film flow is assumed to be laminar, one-dimensional and fully developed hydrodynamically throughout and no shear forces is assumed at the free interface, a Nusselt profile, equation (1), can be used for the film velocity [27].

$$u_f(y_1) = \frac{\rho_f g}{\mu} e_f^{\,2} \left(\frac{y_1}{e_f} - \frac{1}{2} \left(\frac{y_1}{e_f} \right)^2 \right) \tag{1}$$

$$\text{with} \quad u_f(0) = 0 \quad \text{and} \quad \frac{\partial u_f(e_f)}{\partial y_1} = 0$$

The following parameters can be determined knowing the mass flow rate per unit of width of the film.

The mass flow rate per unit of width of the film is given in equation

(2):

$$\Gamma_f = \frac{\dot{m}_f}{l} = \rho_f e_f \overline{u}_f \tag{2}$$

The mean velocity is defined as in equation (3), [28]:

$$\overline{u}_f = \frac{1}{\rho_f A_f} \int \rho_f u_f(y_1) dA_f \tag{3}$$

For a Nusselt profile with constant density, it reduces to equation (4):

$$\overline{u}_f = \frac{1}{e_f} \int u_f(y_1) dy = \frac{\rho_f g}{3\mu_f} e_f{}^2 = \frac{2}{3} u_{f,\,max} \tag{4}$$

From the two above equations, the film thickness can easily be determined through the equation (5):

$$e_f = \left(\frac{3\mu_f \Gamma_f}{\rho_f^2 g} \right)^{\frac{1}{3}} \tag{5}$$

The film Reynolds number is defined as in equation (6):

$$Re_f = \frac{4\Gamma_f}{\mu_f} \tag{6}$$

2.2.2.2. Heat transfer fluid. For the HTF, both mass flow rate per unit of width and the channel thickness are known, thus the mean velocity and the HTF Reynolds number are defined in equation (7) and (8) respectively:

$$\overline{u}_{htf} = \frac{\Gamma_{htf}}{2 e_{htf} \rho_{htf}} \tag{7}$$

$$Re_{htf} = \frac{2\rho_{htf} \overline{u}_{htf} e_{htf}}{\mu_{htf}} \tag{8}$$

For the HTF, the Poiseuille equation is used to determine the velocity profile through the equation (9) with respect to the following: incompressible and Newtonian fluid; high channel length compared to the channel thickness; laminar flow through a constant cross-section and no fluid acceleration:

$$u_{htf}(y_2) = 3\overline{u}_{htf} \left(\left(\frac{y_2}{e_{htf}} \right) - \frac{1}{2} \left(\frac{y_2}{e_{htf}} \right)^2 \right) \tag{9}$$

$$\text{with} \quad u_{htf}(0) = 0 \quad \text{and} \quad \frac{\partial u_{htf}(e_{htf})}{\partial y_2} = 0$$

2.2.3. Thermal model

According to the above hypothesis, the heat balance in the different medium can be expressed as following:

In the falling film, the energy balance is given by the equation (10):

$$\rho_f C_{p,f} u_f(y_1) \frac{\partial T_f(x, y_1)}{\partial x} = \lambda_f \left(\frac{\partial^2 T_f(x, y_1)}{\partial y_1^2} + \frac{\partial^2 T_f(x, y_1)}{\partial x^2} \right) \tag{10}$$

Through the wall, equation (11):

$$\frac{\partial T_w(x, y)}{\partial y} = \frac{T_{htf}(x, e_{htf}) - T_f(x, e_{htf} + e_w)}{e_w} \tag{11}$$

In the HTF, equation (12):

$$\rho_{htf} C_{p,htf} u_{htf}(y_2) \frac{\partial T_{htf}(x, y_2)}{\partial x} = \lambda_{htf} \left(\frac{\partial^2 T_{htf}(x, y_2)}{\partial {y_2}^2} + \frac{\partial^2 T_{htf}(x, y_2)}{\partial x^2} \right) \tag{12}$$

The energy equation on the heat transfer fluid side is solved by assuming a symmetry at the center of the channel. To solve the problem, the followings boundary conditions are considered:

(*continued on next column*)

(*continued*)

At $y_1 = 0$ and $.y_2 = e_{htf}$	$\lambda_{htf} \left(\frac{\partial T_{htf}}{\partial y_2} \right)_{y_2 = e_{htf}} = \lambda_f \left(\frac{\partial T_f}{\partial y_1} \right)_{y_1 = 0}$
At $y_1 = e_f$	$T_f(x, e_f) = T_{sat}$
At $y_2 = 0$	$\left(\frac{\partial T_{htf}}{\partial y_2} \right)_{y_2 = 0} = 0$

2.2.4. Performance parameters

To measure the performance of the falling film evaporator, the following parameters are defined:

- The overall heat transfer coefficient per unit of width is defined as in equations (13) and (14):

$$h_{htf} = \int_0^L \frac{\lambda_{htf} \left(\frac{\partial T_{htf}}{\partial y_2} \right)_{y_2 = e_{htf}}}{\left(T_{bulk,htf}(x) - T_{htf}(x, e_{htf}) \right)} dx \tag{13}$$

$$h_f = \int_0^L \frac{\lambda_f \left(\frac{\partial T_f}{\partial y_1} \right)_{y_1 = 0}}{\left(T_f(x, 0) - T_{bulk,f}(x) \right)} dx \tag{14}$$

$$\text{with} \quad T_{bulk,fluid}(x) = \frac{\iint \rho_{fluid} C_{p,fluid} u_{fluid} T_{fluid}(x, y) dy}{\rho_{fluid} C_{p,fluid} \overline{u}_{fluid} A}$$

where the subscript fluid here can either be the HTF or the falling film.

- The thermal efficiency of the falling film evaporator is classically defined as in equation (15):

$$\varepsilon_{th} = \frac{\dot{Q}_{htf}}{\dot{Q}_{max}} \tag{15}$$

$$\text{with} \quad \dot{Q}_{max} = \dot{m}_{htf} C_{p,htf} (T_{htf,in} - T_{f,in})$$

- The evaporated mass flow rate is calculated at the interface as in equation (16):

$$\dot{m}_{evap} = \frac{\dot{Q}_{f,interface}}{\Delta H_{liq-vap}} \tag{16}$$

$$\text{with} \quad \dot{Q}_{f,interface} = \int_0^l \left(\int_0^L \lambda_f \left(\frac{\partial T_f}{\partial y_1} \right)_{y_1 = e_f} dx \right) dz = l \int_0^L \lambda_f \left(\frac{\partial T_f}{\partial y_1} \right)_{y_1 = e_f} dx$$

- The evaporation efficiency of the falling film evaporator is defined as in equation (17):

$$\varepsilon_{evap} = \frac{\dot{m}_{evap} \Delta H_{liq-vap}}{\dot{Q}_{htf}} \tag{17}$$

$$\text{with} \quad \dot{Q}_{htf} = l \int_0^L \lambda_{htf} \left(\frac{\partial T_{htf}}{\partial y_2} \right)_{y_2 = e_{htf}} dx$$

- The total evaporation rate is defined as in equation (18):

$$\tau_{evap} = \frac{\dot{m}_{evap}}{\dot{m}_f} \tag{18}$$

2.2.5. Entropy generation

2.2.5.1. Local entropy generation. Analysis of irreversibilities in the evaporator is essential to identify, locate and quantify the different sources of entropy generation. Indeed, the second law of thermodynamics provides a measure of entropy generation rate and irreversibilities within a system or process aiming to characterize the efficiency of the transfer process. In this section, the entropy generation at local scale

is described. All along x, negligible pressure drop is assumed. Some extra assumptions are needed in order to formulate the entropy generation namely:

- No chemical reactions.
- Steady state regime of the two-dimensional flow.
- Gravity-driven laminar flow of Newtonian incompressible liquid film.
- The irreversible processes take place near equilibrium

Under the problem formulation and the mentioned assumptions, the entropy generation rate is given by Hirschfelder et al. [29] and Haase [30] as the sum of the product of thermodynamic forces and fluxes – equation (19):

$$\dot{\sigma}_{gen} = \sum_k \vec{X}_k \vec{J}_k \tag{19}$$

with $\vec{X}$ and $\vec{J}$ are the driving force and the flux of the k phenomenon respectively.

In the study case, the only phenomena present are those due to heat transfer and hydrodynamics, as there is no chemical reaction and no mass transfer (the water and vapor are pure), thus the local entropy generation can be written as equation (20):

$$\dot{\sigma}_{gen,fluid} = \underbrace{-\vec{q}_{heat,fluid}\overrightarrow{grad}\left(\frac{1}{T}\right)}_{\text{Thermal entropy}} + \underbrace{\frac{\bar{\bar{\tau}}:\bar{\bar{\nabla}}(\vec{V})}{T}}_{\text{Viscous entropy}} \tag{20}$$

with $\vec{q}_{heat,fluid} = -\lambda_{fluid}\overrightarrow{grad}(T)$ for conductive heat transfer.

By developing the above equation with respect to equations (3) and (5), the local entropy generation can be expressed as in equation (21):

$$\dot{\sigma}_{gen,fluid}(x,y) = \frac{\lambda_{fluid}}{T_{fluid}(x,y)^2}\left[\left(\frac{\partial T_{fluid}(x,y)}{\partial y}\right)^2 + \left(\frac{\partial T_{fluid}(x,y)}{\partial x}\right)^2\right] + \frac{\mu_{fluid}}{T_{fluid}(x,y)}\left(\frac{\partial u_{fluid}(y)}{\partial y}\right)^2 \tag{21}$$

where the subscript fluid here can either be the HTF or the falling film.

2.2.5.2. Overall entropy generation. Here, the overall entropy generation will be defined in two different manners. Firstly, from the local definition by integration and secondly by applying the second law of thermodynamics directly to the whole falling film exchanger.

2.2.5.2.1. Overall entropy generation calculated from local modeling. The global entropy generation is obtained by integration of the equation (21) as following, equation (22):

$$\begin{aligned}\dot{S}_{gen} &= \iiint \dot{\sigma}_{gen} dxdydz \\ &= l\int_0^L \int_0^{e_{htf}} \left(\dot{\sigma}_{gen,htf,th} + \dot{\sigma}_{gen,htf,v}\right) dxdy + l\int_0^L \int_{e_{htf}}^{e_{htf}+e_w} \dot{\sigma}_{gen,w,th} dxdy + l \\ &\times \int_0^L \int_{e_{htf}+e_w}^{e_{htf}+e_w+e_f} \left(\dot{\sigma}_{gen,f,th} + \dot{\sigma}_{gen,f,v}\right) dxdy\end{aligned} \tag{22}$$

The first integral gives the thermal and viscous irreversibilities in the HTF, the second integral represents the thermal irreversibility through the wall – no viscous irreversibility is observed in the wall as the latter is impermeable. The thermal and viscous irreversibility in the film is given by the third integral.

The two contributions of the entropy generation, namely the thermal and viscous entropy generations, could be distinguished as following:

$$\dot{S}_{gen} = \dot{S}_{gen,th} + \dot{S}_{gen,v} \tag{23}$$

The thermal entropy generation is defined in equation (24), while the viscous entropy generation is defined in equation (25).

$$\dot{S}_{gen,th} = \dot{S}_{gen,htf,th} + \dot{S}_{gen,f,th} + \dot{S}_{gen,w,th} \tag{24}$$

$$\dot{S}_{gen,v} = \dot{S}_{gen,htf,v} + \dot{S}_{gen,f,v} \tag{25}$$

2.2.5.2.2. From the second law of the thermodynamics applied to the whole exchanger. By application of the second law of the thermodynamic to the whole falling film exchanger with phase change, the entropy generation is given by the equation (26):

$$\dot{S}_{gen,th} = \dot{m}_{htf} c_{phtf} \ln\left(\frac{T_{htf,out}}{T_{htf,in}}\right) + \frac{\dot{m}_{evap}\Delta H_{liq-vap}}{T_{sat}} + \dot{m}_f c_{pf} \ln\left(\frac{T_{f,out}}{T_{f,in}}\right) \tag{26}$$

The first contribution of the thermal entropy generation in the above equation, represents the entropy variation due to the temperature gradient in the HTF, while the second and third ones represent the entropy variation in the falling film due to the phase change at the film free interface and to the temperature gradient. By using equations (15) and (17), equation (26) can be rewritten as in equation (27):

$$\frac{\dot{S}_{gen,th}}{\dot{m}_{htf} c_{htf}} = ln\left(1 - \varepsilon_{th}\left(1 - \frac{T_{f,in}}{T_{htf,in}}\right)\right) + \varepsilon_{evap}\varepsilon_{th}\left(\frac{T_{htf,in} - T_{f,in}}{T_{sat}}\right) + \frac{1}{R} ln\left(\varepsilon_{th} R(1 - \varepsilon_{evap})\left(\frac{T_{htf,in}}{T_{f,in}} - 1\right) + 1\right) \tag{27}$$

where the dimensionless parameter R is defined as,

$$R = \frac{\dot{m}_{htf} c_{p,htf}}{\dot{m}_f c_{p,f}} \tag{28}$$

3. Resolution method and operating conditions

3.1. Numerical solution

The resolution of the thermal and hydrodynamic models is done by applying a finite difference discretization on the spatial derivative terms using the Julia programming language, then numerically solving the system of non-linear equations obtained using the Trust-Region Method [31] to obtain the solution for a steady state condition. A first-order backward difference is used in the x-direction while a second-order central difference is adopted in the y-direction for both fluids. The numerical domain was discretized into N nodes in the x-direction, M nodes in the y_2-direction and P nodes in the y_1-direction. Initially, a matrix $N \times (M+P)$ that contains the initial HTF temperature in the $N \times M$ and the inlet film temperature in the $N \times P$ is defined. The function developed in the code contains boundary conditions and loop controls. Iteration is required for each step to fill the matrix with the new temperature values until the boundary conditions (paragraph 2.2.3) are satisfied in the steady-state conditions. The absolute and relative tolerance errors are set to have a value of 10^{-6} and 10^{-8} respectively. Knowing the temperature field in both fluids, the evaporated mass flow rate is calculated at the free interface and the local entropy generation is determined in the whole domain.

3.2. Grid size effects

In order to investigate the grid size effect, runs were performed with 160 × (40 + 40), 500 × (40 + 40), 600 × (40 + 40), 750 × (40 + 40), 160 × (30 + 30), 600 × (30 + 30), 750 × (30 + 30) and 750 × (50 + 50). The total evaporated mass is calculated for the different runs, leading to a maximum difference of 2% in terms of evaporated mass flow rate for a reference case $Re_{htf} = 1000$, $Re_f = 49.8$, $e_{htf} = 1$ mm. The 500 × (40 + 40), meshes were chosen in the final calculation as the running time increases from 245 s for 160 × (40 + 40) to 2500 s for 600 × (40 + 40). The chosen meshes have a running time of around 1200 s. However,

Table 1
Main design characteristics of the evaporator.

Configuration	Symbol	Co and counter HTF flow
Evaporator length	L	0.1–0.5 m
Thickness of the wall	$_{ew}$	3×10^{-3} m
Conductivity of the wall	λ_w	500 $W{\cdot}K^{-1}{\cdot}m^{-1}$
Width of the evaporator	l	0.1 m
Thickness of the HTF channel	$2e_{htf}$	$1.75 \times 10^{-3} - 4 \times 10^{-3}$ m

the study of the grid size effect shows that an increase in the flow rate of the HTF requires an increase in the number of meshes in order to remain on results where the maximum difference is 2% in terms of evaporated mass flow rate. Increasing the mesh size means increasing the computation time - about 1*h*10 per simulation for the case of $Re_{htf} = 2000$. Because of the long computation time, the 500 × (40 + 40) has been retained even for simulations different to the reference case, and this even if the maximum deviation of the evaporated mass flow rate is no longer 2% but around 6% for $Re_{htf} = 2000$. To conclude, the mesh size was chosen by making a compromise between the maximal acceptable variation of evaporated mass flow rate and running time. In the following the same mesh grid –500 × (40 + 40) – is used for all simulations.

3.3. Operating conditions

The evaporator considered in this study is an evaporator that can be used in absorption systems for building heating and cooling. The parameters used here are in accordance with the studies carried out in the LOCIE laboratory in the framework of the improvement of absorption machines [32]. The main design characteristics of the evaporator are summarized in Table 1. The behavior of the evaporator is studied by analyzing the impact of the evaporator length on the evaporated mass flow rate, entropy generation and on the thermal and evaporation efficiencies.

The chosen film fluid and HTF for the simulation are both water. Thus, the evaporation temperature T_{sat} is maintained at 300.0 K for a saturation pressure of 3.4 kPa [33] and the evaporation heat (ΔH_{liq_vap}) is 2549 kJ/kg [34]– see appendix for the used equations. Table 2 summarizes the main operating parameters used for the simulation. To study the impact of the falling film and HTF Reynolds numbers on the evaporated mass flow rate, a parametric study was conducted by considering Reynolds number between 49.8 and 200 [32] and between 500 and 2000 for the falling film and the HTF respectively.

The study was made for both co and counter-current configurations with the aim of analyzing their performance and studying the impact of both configurations on the local and overall entropy generation for different film inlet temperature, falling film and heat transfer fluid Reynolds but also for different evaporator length.

3.4. Model validation

For the validation of the model, two different comparison points were considered. The first point is to validate the model by comparing only the thermal entropy generation obtained using equations (22) and (26) for counter-current configuration. Fig. 2 shows the evolution of the thermal entropy generation obtained by integration using the equation (22) with the thermal entropy generation of the equation (27) for different HTF Reynolds number using the design characteristics mentioned in Table 1 and the parameters in Table 2. The film Reynolds number is assumed equal to 49.8, the evaporator length equal to 0.5 m and the HTF channel thickness equal to 2 mm.

The black line represents the ideal case where the entropy generation obtained from equation (22) is equal to the one obtained from equation (27). From this figure, it can be concluded a great agreement between the two entropy generations as the maximum deviation is about 7% and the mean deviation is less than 5%. The deviation when increasing the Reynolds number is linked to the mesh chosen as the test grid has been performed for HTF Reynolds number equal to 10 00. In order to reduce the incertitude and error, in the following section, the parametric analysis is done mainly by assuming a $Re_{htf} = 1000$.

The second point is a comparison of the present work with the analytical results of Flores [26] in order to validate the falling film model by assuming an adiabatic wall and a constant temperature at the

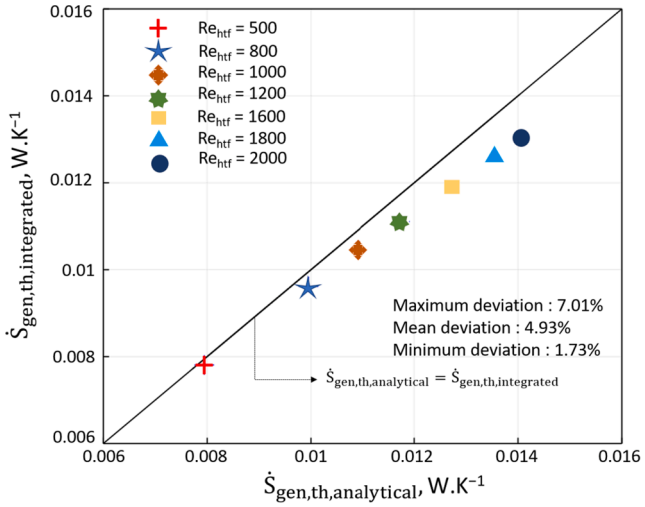

Fig. 2. Comparison of the entropy generations for different Reynolds number and for counter-current configuration.

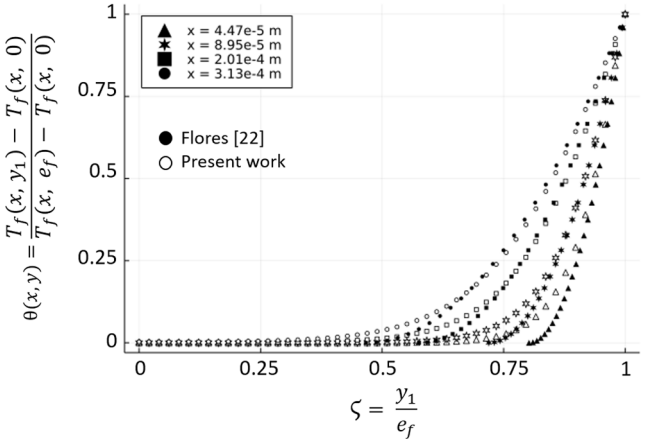

Fig. 3. Validation of the model by comparing the present work with those of Flores during the development of the thermal boundary layer [22].

Table 2
Fluids characteristics [1,35].

	Γ kg. m^{-1}. s^{-1}	λ $W{\cdot}K^{-1}{\cdot}m^{-1}$	ρ $kg{\cdot}m^{-3}$	Cp $J{\cdot}K^{-1}{\cdot}kg^{-1}$	T_{in} K	Re -
HTF	0.4–1.6	0.61	997.5	4178.0	305	500–2000
Film	0.01–0.04	0.61	997.5	4178.0	300–302.5	49.8–200

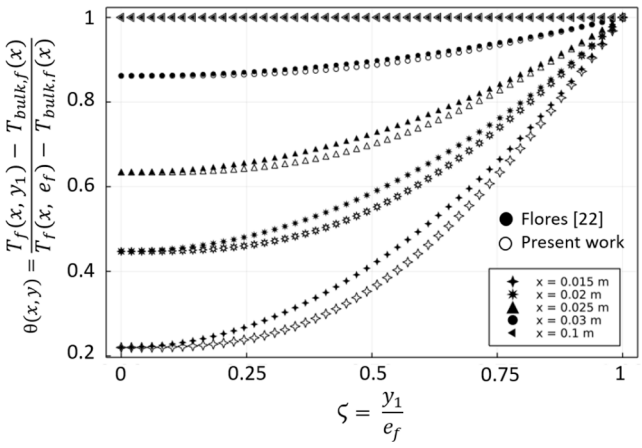

Fig. 4. Validation of the model by comparing the present work with those of Flores in the fully thermally developed region [22].

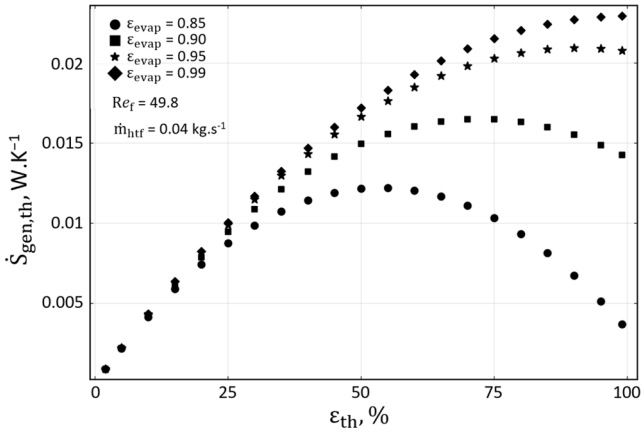

Fig. 5. Evolution the thermal entropy generation with the thermal and evaporation efficiencies.

film interface. The difference of temperature between the interface and the inlet temperature of the film is equal to 2 °C. The comparison is carried out using non-dimensional variables, namely, $\varsigma = \frac{y_1}{e_f}$coordinate in y_1 direction and temperature θ. In Flores [26], the plate length is divided into two parts. Near the entrance of the exchanger corresponds to the part where the thermal boundary layer is not yet fully developed while the second part corresponds to the fully thermally developed region.

In the entrance region, the non-dimensional temperature is defined as in equation (29):

$$\theta = \frac{T_f(x,y_1) - T_f(x,0)}{T_f(x,e_f) - T_f(x,0)} = \left(\frac{e_f - \delta_{f,th}}{\delta_{f,th}}\right)^2 - 2\frac{(e_f - \delta_{f,th})e_f}{\delta_{f,th}^2}\varsigma + \left(\frac{e_f}{\delta_{f,th}}\right)^2\varsigma^2 \quad (29)$$

The evolution of the temperature through the film thickness at different x positions for the entrance region is shown in Fig. 3. As it can be seen, great agreement is observed between the two models as the mean deviations is about 0.7% even if the maximal absolute deviation is 100%. Indeed, at $x = 4.5 \times 10^{-5}$ m and $\varsigma = 0.77$, the non-dimensional temperature obtained by Flores is 0 while the one obtained with the present model is 0.06. The same figure shows that the thermal boundary layer grows more rapidly in the present model than in the one developed by Flores. This result can be explained by the impact of the temperature parabolic profile assumed by Flores.

In the fully developed region, the non-dimensional temperature is defined as bellow:

$$\theta = \frac{T_f(x,y_1) - T_{bulk,f}(x)}{T_f(x,e_f) - T_{bulk,f}(x)} = \frac{T_f(x,0) - T_{bulk,f}(x) + \left(T_f(x,e_f) - T_f(x,0)\right)}{T_f(x,e_f) - T_{bulk,f}(x)}\varsigma^2 \quad (30)$$

Fig. 4 shows the temperature evolution through the film thickness at different x positions. It shows a great agreement between this model and the one developed by [26] mainly far from the inlet of the evaporator. Indeed, the maximum deviation is about 14% and is found near the entrance of the fully developed region. The deviation decreases with the increase of the film length to be almost equal to 0.7% at x = 0.1 m.

4. Results

In this section, results of the present study are presented. First, the analyze of equation (27) is done in order to have an overview of the evolution of the thermal entropy generation with the evaporation and thermal efficiencies at the component scale. Afterwards, a local analysis is performed to deeply understand the local behavior of a falling film evaporator. To do that, the impact of the heat transfer fluid Reynolds number, Re_{htf} = [500 – 2000], falling film inlet temperature, $T_{in,f}$ (K) = {298.00, 299.00, 300.0, 301.0, 302.0, 303.0} and of the film Reynolds number, Re_f = [49.8 – 150], on the evaporation process and entropy generation rate are determined, presented and analyzed for a saturation temperature of 300.0 K and for both heat transfer fluid flow configurations. In the following, only the mass flows and inlet temperatures are assumed the same for both configurations as inputs of the model.

4.1. Overall analysis and reference case

From equation (27), the thermal entropy generation varies with the thermal efficiency, the R-value and the evaporation efficiency. Here, the impact of these parameters on the thermal entropy generation is discussed for a reference case where $Re_f = 49.8$ and $\dot{m}_{htf} = 0.04$ m. s^{-1}. The HTF inlet temperature is equal to 305 K whereas the film inlet temperature is assumed equal to the interface film temperature (300 K). Fig. 5 shows the evolution of the thermal entropy generation with the evaporation and thermal efficiencies using equation (27). The thermal entropy generation increases with the increase of the evaporation efficiencies. The thermal entropy generation also presents a maximum value depending on the thermal efficiency.

For the considered mass flows, the analysis shows that the evaporation efficiency cannot be below 83%. The analysis at component scale of the thermal entropy generation does not give any information about the reason why the evaporator cannot work with an evaporation efficiency lower than 0.83 for high thermal efficiency. Local study is then important in order to have more information on thermal entropy generation sources and evolution.

Fig. 6 shows the evolution of the total entropy generation through the film thickness and along the plate length for the same previous reference case – $2e_{htf}$ = 2 mm, $\dot{m}_{htf}$ = 0.04 m. s^{-1}, HTF Reynolds number of 1000, film Reynolds number of 49.8 and a temperature difference between the inlet and the interface of the film (ΔT) equal to 0. However, the focus is on the thermal entropy generation as the total viscous irreversibilities are 100 times lower compared to the total thermal ones.

In the film, when assuming a temperature difference between the inlet and the interface of the film (ΔT) null, at the entrance, only the thermal boundary layer due to the heat transferred from the HTF to the film is in developing stage, leading to the increase of the film temperature. Inside this thermal boundary layer, thermal irreversibility is observed due to the heat transfer and these irreversibilities are higher near the wall and decrease with the development of the boundary layer. Beyond this thermal boundary layer, no phenomenon occurs, as the film temperature is equal to the interface temperature and thus, no thermal irreversibility is observed. Consequently, for both configurations, the

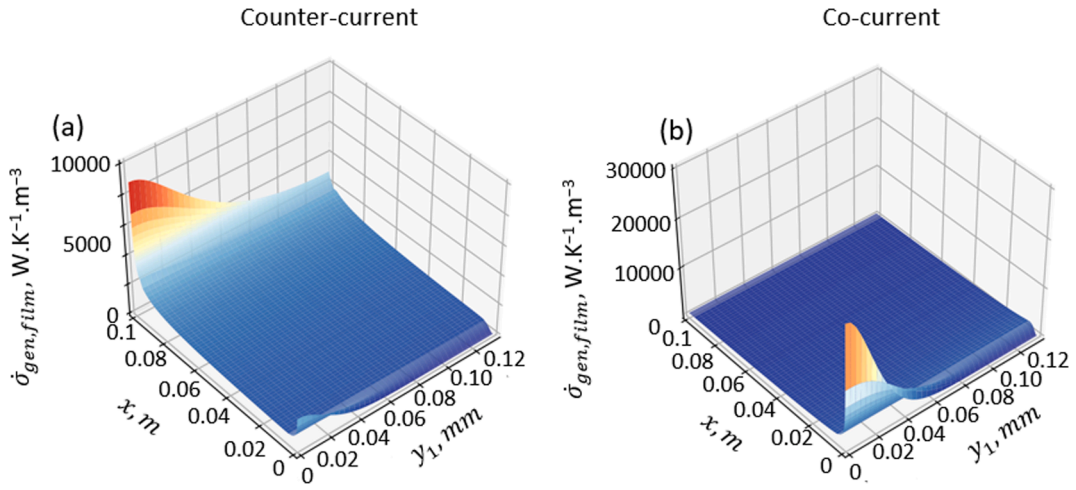

Fig. 6. Thermal entropy generation through the film for both co and counter-current configurations, $Re_{htf} = 1000$, $Re_f = 49.8$, $e_{htf} = 1$ mm and $\Delta T = 0$ K.

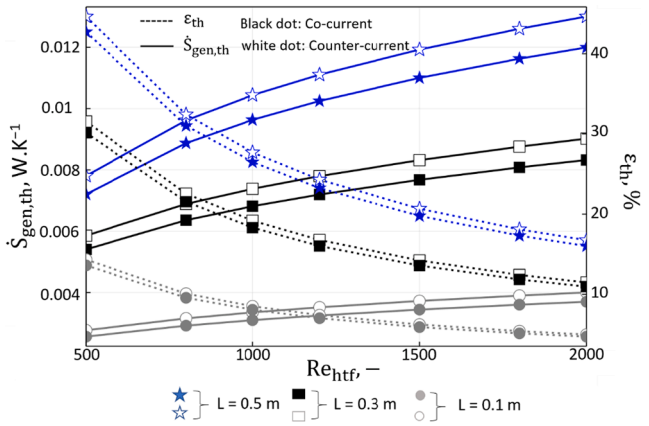

Fig. 7. Overall entropy generation and thermal efficiency versus the heat transfer fluid Reynolds number and the evaporator length for $e_{htf} = 1$ mm and $\Delta T = 0$ K.

main entropy generation is located near the wall$y_1 = 0$ (for the film) where the temperature gradient is higher and so the transfer is larger and this, even after the complete development of the thermal boundary layer in the falling film. Indeed, the irreversibilities are higher near the wall compared to the film interface: the heat transferred from the HTF to the film is high compared to the evaporation phenomenon under the studied conditions. For counter-current, Fig. 6a, the maximal local entropy generation is around 10 000 W. K^{-1}. m^{-3} while for co-current, Fig. 6b, the maximal local entropy generation is around 30 000 W. K^{-1}. m^{-3} (three times higher than in counter-current flow). However, the local entropy generation in the co-current configuration rapidly decreases along the x axis due to the decrease of the heat flux through the wall. The decrease of the heat flux transferred from the HTF to the film also leads to the decrease of the evaporated mass flow rate. For the counter-current flow (Fig. 6a), the entropy generation variation along the x axis is small compared to the entropy generation variation in co-current flow, due to the almost constant small temperature gradient observed in the evaporator with this configuration leading to a slight variation of the heat transfer flux through the wall. Fig. 6a shows that the local entropy generation in the falling has a minimum value in the flow direction corresponding to the position where the thermal boundary layers of both fluids are fully developed.

Moreover, for a considered configuration (counter or co-current), the thermal entropy generation in the HTF and in the film are of the same order of magnitude near the plate – slightly higher in the heat transfer fluid side as shown in appendix, Fig. A1. This is due to the heat flux conservation through the wall and to the fact that both fluids considered are water (same conductivity). In the HTF, a thermal boundary layer is also observed due to the decrease of the temperature linked to the heat flux transferred to the film. Depending on the flow configuration, the thermal boundary layer develops from the top to the bottom or from the bottom to the top. Moreover, due to the fix channel thickness, the laminar HTF flow assumption (leading to a slow development of the thermal boundary layer), the small HTF conductivity, and to the small Prandtl number – around 5 -, the thermal irreversibility within the HTF quickly decreases from the wall to the channel center. The thermal entropy generation through the wall is small. For co-current flow, it varies from around 29 W. K^{-1}. m^{-3} at the entrance to 0.6 W. K^{-1}. m^{-3} at the bottom of the evaporator. However, for counter-current flow, the thermal entropy generation through the wall varies from 11 W. K^{-1}. m^{-3} at the bottom of the evaporator then decreases until reaching a minimal value of around 0.7 W. K^{-1}. m^{-3} before increasing to 3 W. K^{-1}. m^{-3} at the top of the evaporator. In counter flow configuration, the increase of irreversibility observed at the bottom of the falling film evaporator near the wall is due to the thermal boundary layer development and to the large temperature difference between the two sides of the wall caused by the HTF uniform temperature imposed at the bottom of the evaporator. Indeed, this phenomenon implies the existence of a minimum value of the heat flux transferred from the HTF to the film, along the x axis: consequently, a minimum value of thermal entropy generation is also observed. In conclusion, in counter-current flow, the irreversibilities are mainly concentrated near the wall at the bottom of the evaporator ($x = 1$ m, $y_2 = 1$ mm) for the HTF and ($x = 1$ m, $y_1 = 0$) for film and a little near the entrance ($x = 0$, $y_2 = 1$ mm) and ($x = 0$, $y_1 = 0$). However, in co-current flow, the irreversibilities are concentrated near the wall at the entrance of the evaporator ($x = 0$, $y_2 = 1$ mm) for the HTF and ($x = 0$, $y_1 = 0$) for the film.

Knowing the local distribution of the entropy generation, allows to better understand the physical phenomena which induce irreversibilities, and to locate them through the evaporator. It is therefore a way to understand the interest of minimizing entropy generation and to improve the performance of falling film evaporators while minimizing the impact of their irreversibilities on the other components of absorption machines. In the type of falling film evaporators studied here, the main parameters that impact their performance are the HTF Reynolds number and temperature, the vapor pressure, the film inlet temperature and mass flow rate but also the evaporator length and wall thickness. In the following, the focus is to understand how some of the above-mentioned parameters influence the total entropy generation – in the HTF, wall and film – and then to analyze how this impact is done by

Table 3
Evolution of the evaporation mass flow rate, evaporation efficiency and heat transfer coefficients with the HTF Reynolds number and with the evaporator length.

		Evaporation rate %		Evaporation efficiency %		h_f $W \cdot m^{-1} \cdot K^{-1}$		h_{htf} $W \cdot m^{-1} \cdot K^{-1}$	
L m	Re_{htf} -	Co-current	Counter-current	Co-current	Counter-current	Co-current	Counter-current	Co-current	Counter-current
0.1	500	2.18	2.2	97.78	93.33	712	730	244	247
	1000	2.59	2.62	97.68	93.78	713	729	286	290
	1500	2.84	2.89	97.66	94.04	713	729	316	322
	2000	3.03	3.08	97.59	94.22	714	728	341	348
0.3	500	4.93	5.03	99.57	97.09	2132	2156	610	613
	1000	5.99	6.13	99.51	97.35	2134	2156	681	685
	1500	6.66	6.83	99.48	97.42	2135	2156	738	743
	2000	7.16	7.36	99.46	97.6	2136	2156	786	792
0.5	500	7.01	7.2	99.93	98.01	3553	3581	963	966
	1000	8.69	8.93	99.86	98.17	3556	3581	1044	1048
	1500	9.73	10.02	99.83	98.28	3558	3581	1116	1120
	2000	10.51	10.83	99.81	98.40	3559	3581	1178	1183

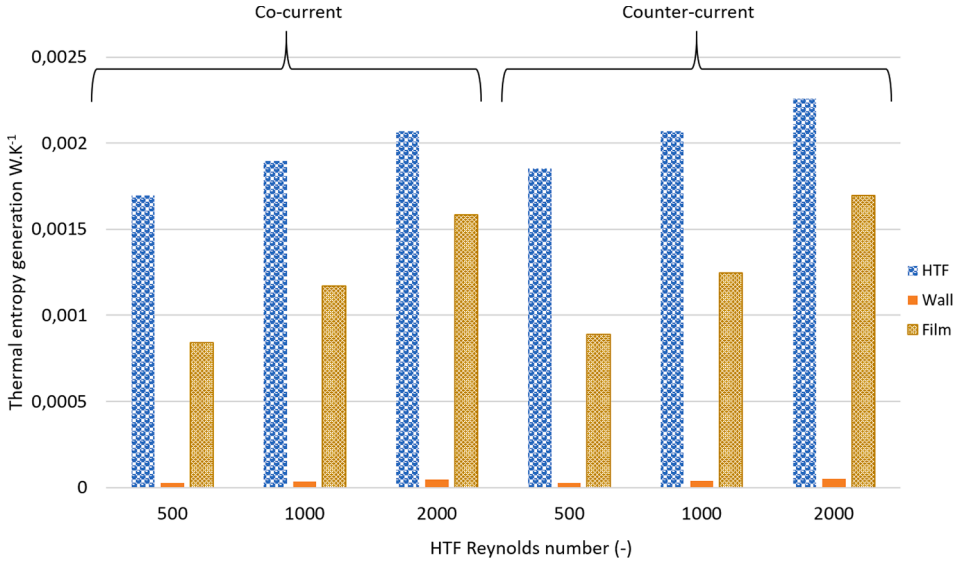

Fig. 8. Evolution of the entropy generation in the HTF, wall and film with the HTF Reynolds number for co-current and counter-current configurations.

studying the local distribution mainly at the region where the entropy generation is the highest.

4.2. *Parametric study*

4.2.1. *HTF Reynolds number influence*

In this section, the impact of the heat transfer fluid mass flow rate on the entropy generation and efficiencies is discussed by varying the HTF Reynolds number. Fig. 7 shows the evolution of the overall thermal entropy generation and of the thermal efficiency with the increase of the heat transfer fluid Reynolds number. For both configurations, the higher the Reynolds number, the higher the overall thermal entropy generation and the lower the thermal efficiency. The increase of the overall entropy generation is due to the increase of the HTF heat capacity. Therefore, the heat flux transferred from the HTF to the film also increases leading to an increase of the evaporated mass flow rate while the decrease of the thermal efficiency is due to the increase of the maximum transferrable flux from the HTF to the film. For a given HTF Reynolds number, the increase of the evaporator length leads to an increase of the total thermal entropy generation and of the thermal efficiency. Moreover, the increase of the HTF Reynolds number from 500 to 2000 increases the entropy generation of about 44%, 51% and 66% for L = 0.1, 0.3 and 0.5 m respectively for both configurations due to the slow development of the HTF thermal boundary layer encountered at high HTF Reynolds number and to the increase of the heat transferred when increasing the evaporator length. Another conclusion is the larger counter-current configuration performance (thermal efficiency) compared to the co-current one with the increase of the evaporator length as expected. Indeed, when considering small evaporator length, there is almost no difference in terms of performance between both configurations – the thermal efficiency difference is less than 5% for $Re_{htf} = 2000$ and L = 0.1 m. It can be concluded that to benefit from the performances offered by the counter-current configuration compared to those offered by the co-current configuration, it is preferable to consider longer falling film evaporators. However, longer evaporators are associated to higher entropy generation that can have significant impact on the other components of the absorption machine. Moreover, other drawbacks such as cost and size must also be considered.

This conclusion is also made by analyzing the evaporation rate for both configurations in Table 3. Indeed, Table 3 shows the evolution of the evaporation mass flow rate and of the evaporation efficiency with the evaporator length and HTF Reynolds number. The Reynolds number of the HTF does not have a large impact on the evaporation efficiency but its increase leads to the increase of the evaporation rate. Indeed, the evaporation efficiency is defined as the ratio of the evaporation flux at the film interface to the transferred flux from the HTF to the film. The increase of the HTF Reynolds number leads to an increase of both terms. However, the amount of energy needed to increase the film temperature

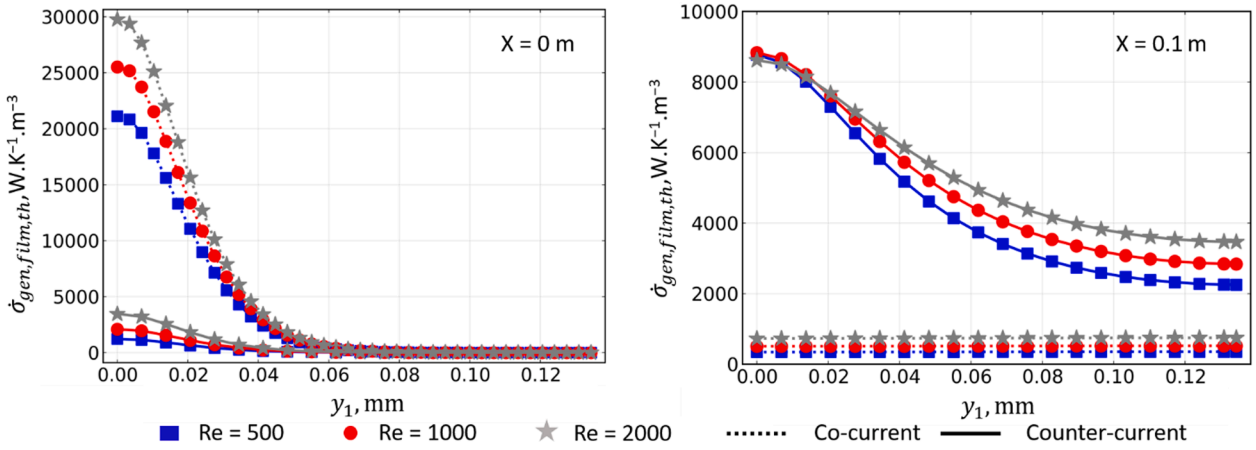

Fig. 9. Evolution of the film thermal entropy generation versus the film thickness for different heat transfer fluid Reynolds number at x = 0 m and x = 0.1 m for ΔT = 0 K for both counter and co – current flows.

is quite the same as the evaporation efficiency mainly depends on the film properties.

The heat transfer fluid and film heat transfer coefficients per unit of width are both calculated from the equations (13) and (14) and are also gathered in Table 3. it shows that the overall heat transfer fluid coefficient of the HTF increases with the increase of its Reynolds number for both configurations. This can be explained by the slow development of the thermal boundary layer when increasing the heat transfer fluid Reynolds number and by the increase of the energy capacity of the HTF. In addition, the analysis shows a higher heat transfer coefficient in the case of counter-current flow due to the small temperature pinch encountered. The higher the heat transfer fluid velocity and the higher the HTF heat transfer coefficient difference between both configurations. The falling film heat transfer coefficient variation is very small, less than 1%, with the increase of the heat transfer fluid velocity for both configurations as the heat transfer coefficient of a fluid depends only on the fluid thermophysical properties (assumed constant), fluid flow (assumed laminar) and exchange configuration. The HTF Reynolds number does not affect the heat transfer coefficient of the film in this case nor the evaporation efficiency; however, it increases the evaporation mass flow rate as the heat transferred through the wall also increases. The evaporator length also impacts significantly the heat transfer coefficient of both fluids – an increase of around 80% when assuming an evaporator length of 0.5 m compared to an evaporator length of 0.1 m. Fig. 8 shows the impact of the HTF Reynolds number on the HTF, wall and film irreversibilities for L = 0.1 m. Under the studied conditions, the highest thermal irreversibility is situated in the HTF, followed by the film. The wall thermal irreversibility represents less than 2% of the total thermal entropy generation. Moreover, the increase of the HTF Reynolds number leads to an increase of the whole thermal irreversibilities. However, it impacts more the film thermal irreversibility than the other irreversibilities due to the increase of the evaporation phenomenon: the contribution of the film thermal irreversibility increases from 32% to 43% of the total thermal entropy generation from Re_{htf} = 500 to 2000 and for both configurations.

It is interesting to understand how the HTF Reynolds number impacts the local thermal entropy generation to understand the result obtained at the component scale. Fig. 9 shows the evolution of the film thermal entropy generation along the film thickness and for different heat transfer fluid Reynolds numbers at the entrance of the evaporator (x = 0 m) and at the bottom (x = 0.1 m) for ΔT = 0 K, Re_f = 49.8, e_{htf} = 1 mm and for both co and counter-current flows.

The increase of the overall thermal entropy generation with the HTF Reynolds number (Fig. 7 et 8) is explained by an increase of the local thermal entropy generation for both configurations as shown in Fig. 9. Indeed, the higher the HTF Reynolds number, the higher the local irreversibility due to the increase of the heat transferred through the wall and consequently the higher is the evaporated mass flow rate: the quick development of the film thermal boundary layer caused by the increase of the HTF velocity – small thermal resistance – allows to evaporate earlier a part of the film. At the entrance near the wall, it is more than six times higher in co-current than in counter-current flow due to the large temperature gradient, while it is equal to zero at the free interface – region not yet impacted by the heat transfer as the thermal boundary layer of the film is still in its developing stage: no phenomenon occurs as the film temperature is equal to the interface temperature. At the bottom (x = 0.1 m), the thermal entropy generation is more than 2 times higher in the counter-current configuration than in co-current one: The heat transferred from the heat transfer fluid to the film is lower in the co-current configuration and the temperature difference is larger in counter current flow. The variation of the thermal entropy generation with the film thickness, at x = 0.1 m, is very small, less than 0.6% whatever the heat transfer fluid Reynolds number in the case of a co-current flow configuration. This result can be explained by the complete development of the thermal boundary layer at x = 0.1 m and by the fact that almost all the energy transferred from the plate to the film is used for the evaporation. Near the wall (y_1 = 0), The variation of the thermal entropy generation with x is higher in the co-current flow due to the monotonically decrease of the heat transferred from the HTF to the film.

The study of the local viscous entropy generation of the two fluids shows – not presented here – that it is no affected by the flow configuration. For the film, the local entropy generation due to the fluid friction is equal to zero at the free interface and increases along the film thickness to be maximal, around 8 W·K^{-1}·m^{-3}, at the wall, y_1 = 0. This result is in accordance with the second term of equation (21) as the velocity profile is parabolic. From the previous results, it can be concluded that the film viscous irreversibilities are negligible compared to the thermal irreversibilities. For the heat transfer fluid, the analysis shows that the local viscous entropy generation depends on the HTF Reynolds number. The increase of the HTF Reynolds number and of the evaporator length lead to a significant impact of the viscous entropy generation contribution on the overall one. Indeed, the contribution of the fluid friction irreversibility on the total entropy generation for L = 0.5 m, under the studied conditions, varies from 4% to 18% and from 3% to 17% for co and counter flows respectively when varying the HTF Reynolds from 500 to 2000. Locally, the HTF viscous entropy generation is equal to zero near the plate which is explained by a velocity equal to zero. This viscous entropy generation increases parabolically, following equation (9), to be maximal at the center of the channel. The local viscous entropy generation along x is almost constant – variation of about 0.4%. It can be concluded that the effect of the local temperature on this viscous

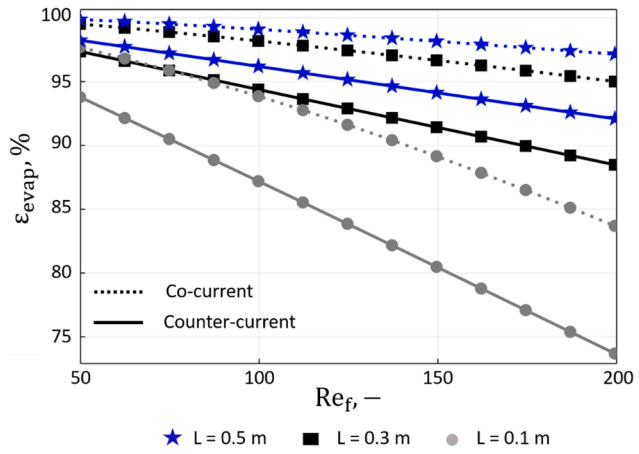

Fig. 10. Evaporation efficiency evolution with the film Reynolds number for different evaporator length.

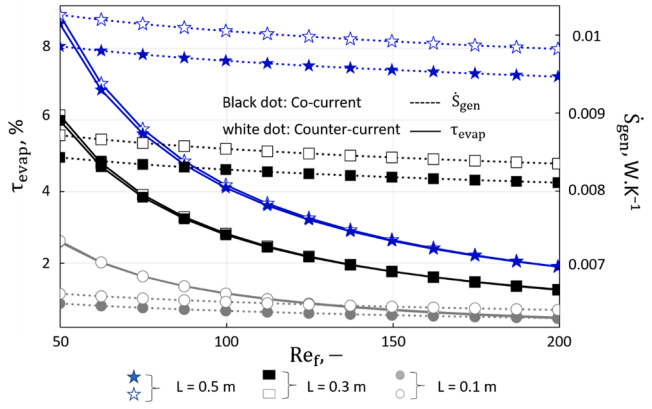

Fig. 11. Evaporation mass flow rate and entropy generation versus the film Reynolds number and for different evaporator length and for Re_{htf} = 1000, e_{htf} = 1 mm and ΔT = 0 K.

irreversibilities is small. The higher the Reynolds number, the higher the local friction irreversibility near the center. To conclude here, the thermal boundary layer plays a significant role on the local entropy generation distribution and consequently on the overall one. The variation of the HTF Reynolds number leads to the variation of the HTF mass flow rate when assuming constant HTF channel thickness, but one could also change the HTF mass flow rate by changing the HTF channel thickness and assuming constant HTF Reynolds number. Thus, both parameters namely the HTF Reynolds number and the channel thickness could be used as parameters of optimization to find the optimal geometry and heat transfer fluid velocity that will lead to a minimal overall entropy generation and an acceptable evaporation rate.

4.2.2. *Film Reynolds number influence*

In this section, the impact of the film Reynolds number on the falling film evaporator is studied. The analysis is limited at the overall scale as the distribution at local scale of the irreversibilities are similar as those studied previously in Section 4.2.1. The HTF Reynolds number is maintained at 1000, the channel thickness is equal to 2 mm and the film inlet temperature is assumed to be equal to the interface temperature (saturation temperature). As in the previous analysis, the difference of temperature between the film and HTF inlet temperatures is about 5 °C. Fig. 10 shows the impact of the film Reynolds number on the evaporation efficiency. The latter decreases with the increase of the film velocity and with the decrease of the evaporator length. Indeed, increasing the film Reynolds number leads to an increase of the film thickness and thus

Table 4
Evolution of the evaporation mass flow rate and evaporation efficiency with the HTF Reynolds number and with the evaporator length.

		h_f W·m^{-1}·K^{-1}		h_{htf} W·m^{-1}·K^{-1}	
L m	Re_f -	Co-current	Counter-current	Co-current	Counter-current
0.1	50	713	730	286	290
	100	570	597	284	293
	150	504	538	282	295
	200	466	506	280	297
0.3	50	2134	2156	681	685
	100	1695	1732	682	690
	150	1484	1533	681	693
	200	1353	1412	679	696
0.5	50	3557	3581	1044	1048
	100	2823	2865	1046	1054
	150	2468	2524	1047	1059
	200	2245	2315	1046	1062

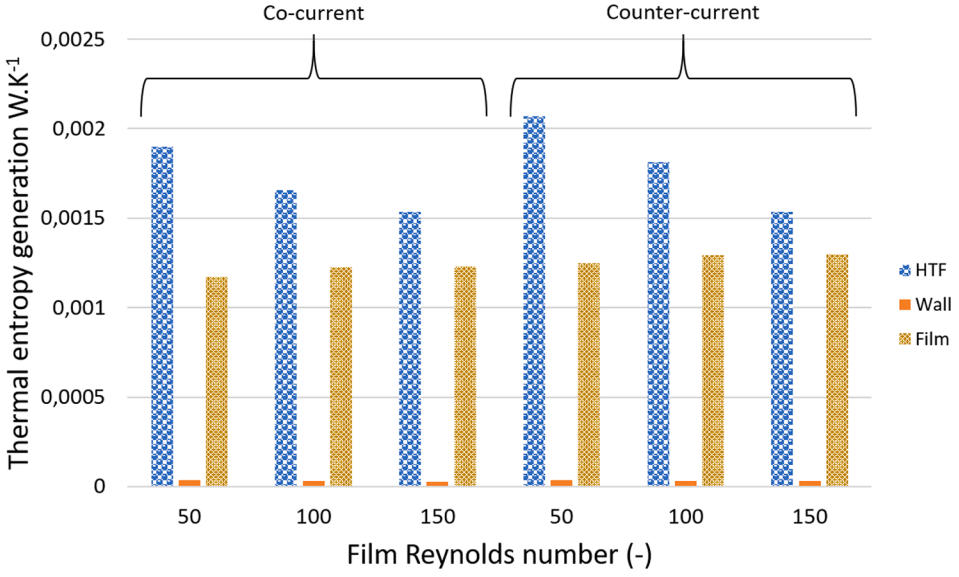

Fig. 12. Evolution of the HTF, wall and film thermal entropy generation for different film Reynolds number and for both configurations.

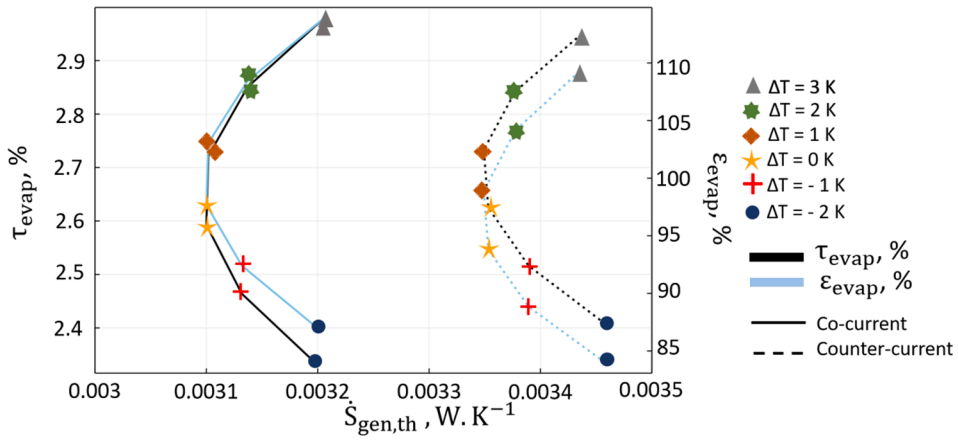

Fig. 13. Thermal entropy generation versus the evaporation efficiency and the total evaporation for different film inlet temperature, $Re_{htf} = 1000$ and $e_f = 1$ mm.

Table 5
Evolution of the evaporation mass flow rate and evaporation efficiency with ΔT and with the evaporator length.

		τ_{evap} %		h_f W·m^{-1}·K^{-1}		h_{htf} W·m^{-1}·K^{-1}	
L m	ΔT K	Co-current	Counter-current	Co-current	Counter-current	Co-current	Counter-current
0.1	-2	2.3	2.4	723	752	280	294
	0	2.59	2.62	713	729	285	290
	2	2.85	2.84	703	705	292	284
	3	2.97	2.95	698	692	296	280
0.3	-2	5.74	5.93	2145	2188	675	689
	0	5.99	6.13	2134	2156	678	685
	2	6.24	6.3	2124	2125	688	678
	3	6.36	6.43	2119	2109	691	672
0.5	-2	8.45	8.75	3567	3617	1038	1052
	0	8.7	8.93	3556	3581	1044	1048
	2	8.93	9.13	3547	3547	1051	1041
	3	9.05	9.22	3542	3531	1055	1034

to an increase of the thermal resistance, consequently more of the energy transferred from the HTF to the film is used to increase the film temperature – 6% of the transferred energy is used to increase the film temperature in counter-current flow for $Re_f = 50$ and L = 0.1 m against 27% for $Re_f = 200$. The difference of the evaporation efficiency is smaller when considering a co-current flow as only 3% of the transferred energy is used to increase the film temperature for $Re_f = 50$ and L = 0.1 m against 16% for $Re_f = 200$. Moreover, the higher the evaporator length, the higher the evaporation efficiency. Consequently, for an infinite evaporator length, the evaporation efficiency would be equal to 1. The smaller the evaporator length, the higher the difference of the evaporation efficiency between both configurations and between $Re_f = 50$ and $Re_f = 200$. The evaporation efficiency is higher for co-current flow than for counter-current flow.

As shown in Fig. 5, the evaporation efficiency cannot be lower than 0.83 for $Re_f = 50$, $\dot{m}_{htf} = 0.04$ m. s^{-1}. Indeed, the evaporation efficiency decreases either by considering small evaporator length or by increasing the film thickness (film Reynolds number). However, for an evaporator length of 0.1 m and $Re_f = 50$, the evaporation efficiency is already up to 0.9 for both configurations which means that there is no evaporator length that leads to a lower evaporation efficiency with a high thermal efficiency.

The decrease of the evaporation efficiency due to the increase of the film Reynolds number leads to a decrease of the entropy generation and evaporation mass flow rate as shown in Fig. 11. Moreover, increasing the evaporator length leads to an increase of the difference between $Re_f = 50$ and 200. Indeed, the increase of the film Reynolds number, from 50 to 200, leads to a decrease of the entropy generation of about 8 % for L = 0.1 m against 14% for L = 0.5 m for a co – current flow. For high film Reynolds numbers, almost no difference is noticed for both configurations in term of evaporated mass flow due to the high thermal resistance between the plate and the film that leads to the slow thermal boundary layer development. In order to take advantage of the flow configuration impact at high film Reynolds number, engineers should also work at high HTF Reynolds number however that also means increasing the

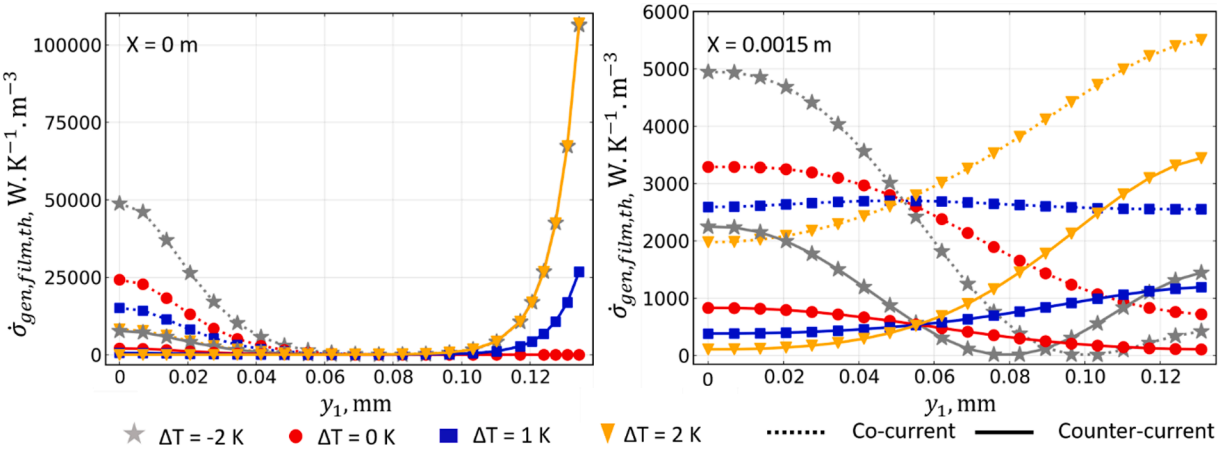

Fig. 14. Evolution of the film thermal entropy generation versus the film thickness for different inlet film temperature at x = 0 m and x = 0.0015 m for counter-current and co-current flow configurations ($T_{htf,\ in} = 305$ K, $T_{f,interface} = 300$ K).

thermal entropy generation as explained in the Section 4.2.1.

The analysis of the viscous entropy generation shows an increase of the latter with the increase of the film Reynolds number and evaporator length. However, the contribution of the total viscous irreversibilities on the total entropy generation remains negligible. Indeed, for $Re_f = 50$, this contribution is about 0.4% and 0.7% for L = 0.1 m and L = 0.5 m respectively against 0.8% and 1.3% for $Re_f = 200$.

The study of the thermal efficiency shows a decrease of the latter with the increase of the film Reynolds number as the film velocity has an impact on the energy transferred by the HTF to the film. However, this decrease is small – for counter flow, the thermal efficiency is 27.7% and 25.16% for ($Re_f = 50$, L = 0.5 m) and ($Re_f = 200$, L = 0.5 m) respectively against 26.5% and 23.8% for co-current flow.

The distribution of the thermal irreversibilities within the HTF, wall and the film are given in Fig. 12. Unlike to the results obtained when studying the impact of the HTF Reynolds number, the increase of the film Reynolds number leads to the decrease of HTF thermal irreversibility while the film irreversibility is slightly affected. The decrease of the HTF irreversibility is due to a decrease of the heat transferred from the HTF to the film caused by the slow development of the thermal boundary layer within the film due to the increase of the film thickness and consequently by the increase of the thermal resistance. This also explains the slight increase of the film thermal irreversibility. Indeed, the film thermal irreversibility goes from around 37% of the total thermal entropy generation for $Re_f = 50$ to 43% for $Re_f = 150$ while the HTF irreversibility decreases from 61% to 53% for $Re_f = 50$ to $Re_f = 150$ respectively.

The wall irreversibility contribution remains negligible less than 1.5%. In conclusion, the wall is the medium with the less entropy generated.

Table 4 gives the heat transfer coefficient of the film and of the HTF for different film Reynolds number. The film heat transfer coefficient increases of about 35% with the decrease of the film Reynolds number – from 200 to 50 – due to the decrease of the thermal resistance. The heat transfer coefficient of the HTF also increase with the decrease of the film Reynolds number; However, its impact is low – less than 3%.

In conclusion, the film Reynolds number plays a significant role on the transfer phenomenon as increasing it leads to a low evaporator performance – the entropy generation variation is small and linear while the evaporation rate decrease is significative. It can also be concluded from paragraph 4.2.1 and 4.2.2 that for laminar HTF flow regime, the main thermal irreversibility of a falling film evaporator is concentrated in the HTF, followed by the film thermal irreversibility, while the wall irreversibility is almost negligible.

In this study, the film Reynolds number is limited to 200 as higher to that value, the film could not be considered laminar anymore and the developed model is not adapted for wavy films. When designing the falling film evaporator, engineers should determine the adequate film Reynolds number by considering HTF characteristic and operating conditions.

4.2.3. Influence of the temperature difference between the film inlet and the interface temperature

In this section the impact of the film inlet temperature is studied. Indeed, the film inlet temperature can be controlled by adjusting the operating conditions of the other components of absorption machines while the interface temperature of the evaporator can be controlled by assuming a constant vapor pressure. The evolution of the overall thermal entropy generation with the evaporation rate and with the evaporation efficiency by considering different film inlet temperatures (298 to 303 K) and constant interface temperature (300 K) is shown in Fig. 13. The subcooled film leads to the highest thermal entropy generation and the lowest evaporation rate. This is due to the high temperature gradient between the HTF and the film leading to a decrease of the evaporation efficiency. That means that a large part of the energy transferred from the HTF to the film serves only to increase the film temperature. The thermal entropy generation created by the temperature difference between the film inlet temperature and the saturation temperature plays also an important role on the film thermal entropy generation. To have efficient evaporator, engineers should avoid subcooled film at the entrance in most applications. The analysis also shows that the minimum thermal entropy generation is encountered when the $\Delta T = 1$ K under the considered conditions. Indeed, with this small difference, the thermal entropy generation through the wall is reduced compared to the case where $\Delta T = 0$ K and the local irreversibilities created near the interface due to the overheating of the film has a small contribution on the overall thermal entropy generation.

However, the higher the film inlet temperature, the lower the thermal entropy generation near the wall and the higher the one at the interface. Thus, even if the overheating leads to a significant increase of the evaporation rate due to a high evaporation efficiency, the optimal temperature difference should be found in order to avoid high total entropy generation. Indeed, for overheated films, the evaporation efficiency is more than unity as in its definition the energy transported by the film at the inlet is not considered. It is up to the engineer to find comprise between the acceptable entropy generation and evaporation rate mainly if the evaporator is in conjunction with other components and can lead to a higher overall entropy generation and consequently to a lower system performance.

The larger the evaporator length and the lower the impact of the inlet film temperature on the evaporated mass flow rate (Table 5). Moreover, the thermal efficiency is significantly impacted by the inlet film temperature – not shown. Indeed, the decrease of the film inlet temperature from 303 to 298 K leads to a decrease of 70% of the thermal efficiency for both configurations whatever the evaporator length.

The film inlet temperature has also an impact on the heat transfer coefficients as shown in Table 5. The heat transfer coefficient of the HTF decreases almost linearly with the increase of the film inlet temperature for a counter-current flow while the opposite trend is found for the co-current configuration. The heat transfer coefficient of the film decreases with the increase of the film inlet temperature for both configurations. However, the impact of the film inlet temperature remains low for both fluids – less than 5%.

The analyze of the behavior of the film when the latter is subcooled or overheated at the entrance of the evaporator gives more details about the distribution of the irreversibilities. The impact of the overheated and subcooled film is mainly observed near the entrance when the thermal boundary layer due to the transfer of energy from the HTF to the falling film is still in the developing stage, as shown in Fig. 14 for a HTF Reynolds number of 1000, a channel thickness of 2 mm and a film Reynolds number of 49.8. It can be seen that at x = 0 m and near the wall ($y_1 = 0$), the local thermal entropy generation is high when the film inlet temperature is subcooled and decreases with the increase of ΔT, for both configurations. Indeed, the higher the temperature difference between the inlet film and the HTF temperature, the higher the local entropy generation near the wall due to the large temperature gradient and the thermodynamic disequilibrium. At the top, two thermal boundary layers are in developing stage. The first one is the thermal boundary layer caused by the heat flux transferred from the HTF to the film while the second one is the thermal boundary layer caused by the evaporation phenomenon at the free interface. This can be observed in Fig. 14 at the top (x = 0 m): the thermal entropy generation is null between $y_1 = 0.05$ mm and $y_1 = 0.09$ mm.

Moreover, when overheating or subcooling the film at the entrance, there is a significant disequilibrium near the free surface due to the temperature difference between the film inlet temperature and the saturation temperature: the local entropy generation is up to 100 000 $W{\cdot}K^{-1}{\cdot}m^{-3}$ for $|\Delta T| = 2$ K against zero for $\Delta T = 0$ K. Indeed, at $\Delta T = 0$ K, there is no heat transfer and consequently no evaporation occurs at the free interface. However, the overheating allows evaporating a part of the falling film whereas the subcooling leads to the condensation of the saturated vapor. At x = 0.0015 m, the inflexion point at the middle of the

film thickness is explained by the thermal boundary layer development due to the heat transferred from the HTF to the film and by the evaporation/condensation phenomenon that already occurs at the free interface due to the overheated/subcooled film.

In terms of configuration, no differences are observed at $x = 0$ m, near the interface ($y_1 = 0.13$ m), this is due to the fact that the thermal boundary layer is not fully developed and so, the impact of the flow configuration is not felt: the irreversibilities observed, at the entrance near the interface, are only due to the evaporation/condensation that occurs when the film is overheated or subcooled. However, differences are observed near the wall where the local thermal entropy generation in co-current flow is higher than that of the counter-current flow. At $x = 0.0015$ m, the film is still in its developing stage but the difference between the local entropy generations decreases. For $\Delta T = -2$ K, the thermal entropy generation is drastically reduced near the interface as the temperature already tends to the interface temperature. Once the film temperature near the interface is equal to the interface temperature, the condensation process stops. The evaporation phenomenon starts once the film temperature near the interface is higher than the interface temperature.

At the bottom of the evaporator ($x = 0.1$ m), the impact of overheating/subcooling the film at the inlet is not at all observed – thermal boundary layer completely developed – and the local thermal entropy generation is higher in counter-current than in co-current flow. The analysis of the thermal entropy generation along the x axis shows that less than 20% of the x axis is impacted by the overheating/subcooling of the film. Moreover, under the studied conditions, the analysis shows that the film inlet temperature impacts the thermal entropy generation of the heat transfer fluid only near the wall and is very small elsewhere.

The impact of the film inlet temperature on the viscous entropy generation of the film is very small. Indeed, the viscous entropy generation decreases with the increase of the film inlet temperature. However, the difference of the viscous entropy generation in the film for $T_{in,f} = 300.0$ K and $T_{in,f} = 302.5$ K is less than 0.01%.

To summarize, although the increase of the film inlet temperature leads to an increase of the evaporated mass flow, the thermal entropy generation should be studied in order to find the film inlet temperature that should be considered to minimize the thermal entropy generation mainly when the falling film evaporator is used in cofunction with other system – as it has an impact on the whole system performance. Moreover, the local analysis shows that at the entrance of the evaporator, the behavior of the latter due to the film inlet temperature – at the free interface ($x = 0$, $y_1 = 0.13$ m) – is the same whatever the flow configuration.

5. Conclusions

The present work deals with the study of a laminar falling film evaporator in the case where the plate is heated by a HTF and for co and counter-current HTF flow configurations. A 2D-model was developed to determine the local temperature and entropy generation. The aim of this study is to evaluate the effect of the operating conditions, namely, the inlet film temperature and film/HTF Reynolds number but also, of the design conditions, namely, the film length on the evaporation rate and on the overall and local entropy generations. The impact of the above-mentioned parameters on the entropy generation was investigated at the overall scale and an analysis was performed at the local scale for a deep understanding of the thermal entropy generation distribution. Different parameters were defined to evaluated the performance of the considered evaporator, namely the evaporator efficiency, total evaporation mass flow rate and the thermal efficiency. The analysis was carried out using a thermodynamic approach in order to evaluate the sources of entropy generation, the contribution of each source on the global entropy generation and the impact of the different parameters on it.

The overall entropy generation increases with the increase of the temperature difference between the free surface and the film at the entrance, and with the increase of the Reynolds number of the HTF for both configurations. The analysis shows that the overall thermal entropy generation is mainly due to the irreversibility within the HTF followed by those within the film, while the irreversibility observed through the wall remains negligible – around 2%. The HTF irreversibility increases with the increase of the HTF Reynolds number while it decreases with the increase of the film Reynold number for co and counter flow configurations. Differences between both flow configurations are mainly observed at longer evaporator length. A decrease of the overall entropy generation and of the evaporation mass flow rate is observed when increasing the film Reynolds number due the increase of the thermal resistance between the HTF and the film. To avoid the decrease of the evaporation mass flow for higher film Reynolds number, a higher HTF Reynolds number must be considered. However, other influence parameters must be studied to keep acceptable entropy generation. The impact of the thermal boundary layers on the local phenomena and consequently on the local and thus overall entropy generation has been investigated. The sources of entropy generation in falling film evaporator are the fluid friction and the temperature gradient. The local viscous entropy generation of the film and of the HTF are almost not impacted by the film inlet temperature and by the film Reynolds number. However, the HTF Reynolds number impacts the HTF local viscous entropy generation and consequently its contribution to the overall entropy generation. Furthermore, the increase of the film inlet temperature leads to an increase of the local thermal entropy generation near the free surface while it leads to a decrease of this entropy generation near the wall. The analysis confirms that the counter-current configuration has a higher performance in terms of evaporation mass flow rate compared to the co-current one due to the almost constant temperature gradient encountered in counter-current flow and that, even if the entropy generated in the counter-current flow is higher than those generated in a co-current flow. That means that higher entropy generation does not mean lower efficiency but a comprise between both must be found.

In terms of perspectives, it would be interesting to include a mass transfer, by assuming no pure vapor, in the analysis of the evaporator in order to understand the thermal and mass coupling effect on the evaporation process and on the entropy generation. The study could also be extended to the analysis of the entropy generation during the absorption phenomenon in an absorber.

CRediT authorship contribution statement

Mahamoudou Arnat: Methodology, Software, Visualization, Formal analysis, Writing – original draft. **Ramousse Julien:** Methodology, Writing – review & editing, Resources, Supervision, Project administration. **Cellier Nicolas:** Software, Writing – review & editing. **Le Pierrès Nolwenn:** Methodology, Writing – review & editing, Resources, Supervision, Project administration.

Declaration of Competing Interest

The authors declare that they have no known competing financial interests or personal relationships that could have appeared to influence the work reported in this paper.

Acknowledgement

The authors would like to acknowledge the Savoie Mont-Blanc University for a financial support.

The authors would like to thank the 15th International Conference on Heat Transfer, Fluid Mechanics and Thermodynamics (HEFAT2021) for allowing to submit this paper as a special issue to the Applied thermal Engineering, after the HEFAT2021 conference, presented online in July 26-28, 2021.

Appendix

The correlation for the equilibrium (saturated) condition at the interface between the water film and the water vapor obtained by [33] is indicated below:.

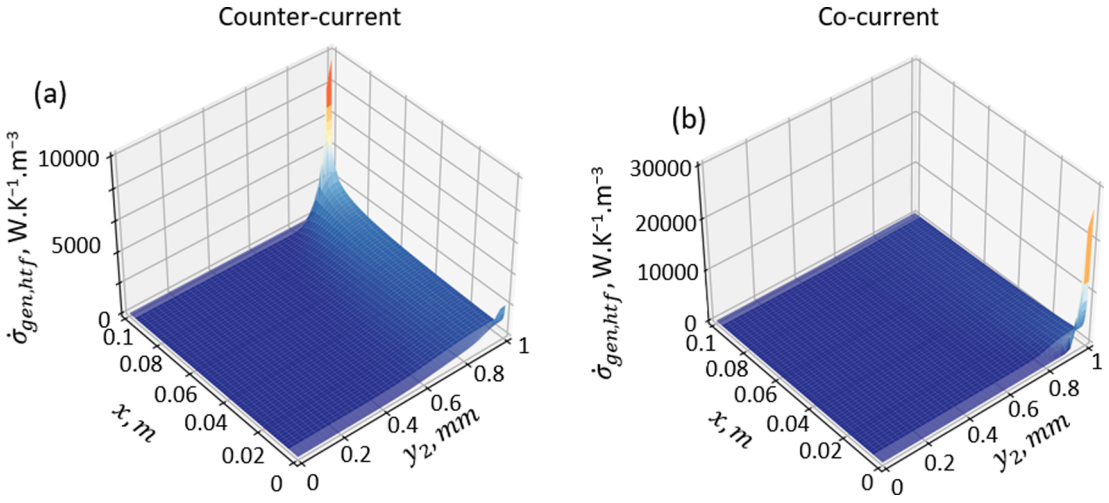

Fig. A1. Thermal entropy generation through the HTF for both co and counter-current configurations, $Re_{htf} = 1000$, $Re_f = 49.8$, $e_{htf} = 1$ mm and $\Delta T = 0$ K.

$$T_{vap,sat}(P_{sat}) = (3.37595948586144E-5) \times \left(\log\left(\frac{P_{sat}}{22064000}\right)\right)^6$$
$$+ (2.12003737295472E-3) \times \left(\log\left(\frac{P_{sat}}{22064000}\right)\right)^5$$
$$+ (5.91993855043397E-2) \times \left(\log\left(\frac{P_{sat}}{22064000}\right)\right)^4$$
$$+ 0.976561958843236 \times \left(\log\left(\frac{P_{sat}}{22064000}\right)\right)^3$$
$$+ 10.767649771597 \times \left(\log\left(\frac{P_{sat}}{22064000}\right)\right)^2$$
$$+ 88.0085016175992 \times \left(\log\left(\frac{P_{sat}}{22064000}\right)\right)^3$$
$$+ 373.128542324967$$

The saturated water–vapor enthalpy correlation obtained by [34] is indicated below:

$$h_{vap,sat} = -0.00125397 \times T_{vap,sat}^2 + 1.88060937 \times T_{vap,sat} + 2500.559$$

References

[1] W.M. Salvagnini, M.E.S. Taqueda, A Falling-Film Evaporator with Film Promoters, Ind. Eng. Chem. Res. 43 (21) (2004) 6832–6835, https://doi.org/10.1021/ie0307636.

[2] M. Ma, J. Yu, X. Wang, and Wng, Performance evaluation and optimal configuration analysis of a CO_2/NH_3 cascade refrigeration system with falling film evaporator–condenser, Energy Convers. Manage. 79 (2014) 224–231, https://doi.org/10.1016/j.enconman.2013.12.021.

[3] L. Gong, S. Zhou, Y. Guo, S. Shen, Distribution of brine temperature in a large-scale horizontal-tube falling film evaporator, Appl. Therm. Eng. 164 (2020) 114437, https://doi.org/10.1016/j.applthermaleng.2019.114437.

[4] E.D. Rogdakis, V.D. Papaefthimiou, D.C. Karampinos, A realistic approach to model LiBr–H_2O smooth falling film absorption on a vertical tube, Appl. Therm. Eng. 23 (17) (2003) 2269–2283, https://doi.org/10.1016/s1359-4311(03)00188-1.

[5] H. Auracher, A. Wohlfeil, F. Ziegler, A simple physical model for steam absorption into a falling film of aqueous lithium bromide solution on a horizontal tube, Heat Mass Transf. 44 (12) (2008) 1529–1536, https://doi.org/10.1007/s00231-008-0386-4.

[6] H. Chen, R.S. Jebson, Factors Affecting Heat Transfer in Falling Film Evaporators, Food Bioprod. Process. 75 (2) (1997) 111–116, https://doi.org/10.1205/096030897531423.

[7] W.M. Kays, A.L. London, E.R.G. Eckert, Compact Heat Exchangers, ASME. J. Appl. Mech. 27 (2) (1960) 377, https://doi.org/10.1115/1.3644004.

[8] R. Marek, J. Straub, Analysis of the evaporation coefficient and the condensation coefficient of water, International Journal, Heat Mass Transf. 44 (1) (2001) 39–53, https://doi.org/10.1016/s0017-9310(00)00086-7.

[9] Liang Pu, Qiang Li, Xiangyu Shao, Lan Ding, Yanzhong Li, Effects of tube shape on flow and heat transfer characteristics in falling film evaporation, Appl. Therm. Eng. 148 (2019) 412–419, https://doi.org/10.1016/j.applthermaleng.2018.11.043.
[10] Chuang-Yao Zhao, Di Qi, Wen-Tao Ji, Pu-Hang Jin, Wen-Quan Tao, A comprehensive review on computational studies of falling film hydrodynamics and heat transfer on the horizontal tube and tube bundle, Appl. Therm. Eng. 202 (2022) 117869, https://doi.org/10.1016/j.applthermaleng.2021.117869.
[11] Nusselt, Die oberflächenkondensation des wasserdampfes, Z Vereines Deutsch Ing 60 (1916) 541–546.
[12] Jesse D. Killion, S. Garimella, A critical review of models of coupled heat and mass transfer in falling film absorption, Int. J. Refrig. 24 (8) (2001) 755–797, https:// doi.org/10.1016/s0140-7007(00)00086-4.
[13] A. Mahamoudou, N. Le Pierrès, J. Ramousse, Review of Coupled Heat and Mass Transfer Studies in Falling Film Absorbers: Modeling, Experimental and Thermodynamic Approaches, Int. J. Refrig. 136 (2022) 229–244, https://doi.org/10.1016/j.ijrefrig.2022.01.024.
[14] G. Karimi, M. Kawaji, An experimental study of freely falling films in a vertical tube, Chem. Eng. Sci. 53 (20) (1998) 3501–3512, https://doi.org/10.1016/s0009-2509(98)00159-6.
[15] W. Ambrosini, N. Forgione, F. Oriolo, Statistical characteristics of a water film falling down a flat plate at different inclinations and temperatures, Int. J. Multiph. Flow 28 (9) (2002) 1521–1540, https://doi.org/10.1016/s0301-9322(02)00039-3.
[16] S. Ben Jabrallah, A. Belghith, J.P. Corriou, Convective heat and mass transfer with evaporation of a falling film in a cavity, Int. J. Therm. Sci. 45 (1) (2006) 16–28, https://doi.org/10.1016/j.ijthermalsci.2005.05.001.
[17] J.S. Prost, M.T. González, M.J. Urbicain, Determination and correlation of heat transfer coefficients in a falling film evaporator, J. Food Eng. 73 (4) (2006) 320–326, https://doi.org/10.1016/j.jfoodeng.2005.01.032.
[18] Zhou, Yu, Gao, An experimental study of falling film evaporation in vertical channels with perforated fins of a plate-fin heat exchanger, Chem. Eng. Process. - Process Intensif. 145 (2019), https://doi.org/10.1016/j.cep.2019.107672.
[19] R. Krupiczka, Ziobrowski, Rotkegel, Heat transfer to evaporating liquid films within a vertical tube, Chem. Eng. Process. Process Intensif. 41 (1) (2002) 23–28, https://doi.org/10.1016/s0255-2701(00)00158-6.
[20] R. Gorla, D. Pratt, Second Law Analysis of a non-Newtonian Laminar Falling Liquid Film Along an Inclined Heated Plate, Entropy 9 (1) (2007) 30–41, https://doi.org/10.3390/e9010030.
[21] O.D. Makinde, Irreversibily analysis for gravity driven Non-Newtonian liquid film along an inclined isothermal plate, Phys. Scr. 74 (6) (2006) 642–645, https://doi.org/10.1088/0031-8949/74/6/007.
[22] Saouli, Aiboud-Saouli, Second law analysis of laminar falling liquid film along inclined heated plate, Int. Commun. Heat Mass Transf. 31 (6) (2004) 879–886, https://doi.org/10.1016/s0735-1933(04)00074-0.
[23] A. Gonda, P. Lancereau, P. Bandelier, L. Luo, Y. Fan, S. Benezech, Water falling film evaporation on a corrugated plate, Int. J. Therm. Sci. 81 (2014) 29–37, https://doi.org/10.1016/j.ijthermalsci.2014.02.010.
[24] Huaylla, Storage of solar energy by absorption: process experimentation and modeling, Ph.D thesis, Communauté Université Grenoble Alpes, 2017. https://tel.archives-ouvertes.fr/tel-02050102.
[25] Kalliadasis, RuyerQuil, Scheid, Velarde, Falling Liquid Films, Springler, New York, 2012, https://doi.org/10.1007/978-1-84882-367-9.
[26] Flores, Etude des transferts de masse et de chaleur au sein d'un absorbeur eau/bromure de lithium, Ph.D thesis, Université de Grenoble, 2014. https://tel.archives-ouvertes.fr/tel-01062936.
[27] Brauner, Non-isothermal vapour absorption into falling film, Int. J. Heat Mass Transf. 34 (3) (1991) 767–784, https://doi.org/10.1016/0017-9310(91)90124-w.
[28] Incropera, Dewitt, Bergman, and Lavine, fundamentals of heat and mass transfer, Sixth, 2006.
[29] Hirschfelder, Curtiss, Bird, The Molecular Theory of Gases and Liquids, Cambridge University Press, vol. 120, 1954. https://doi.org/10.1126/science.120.3131.1097.
[30] Haase, Thermodynamics of irreversible processes (Addison-Wesley, Reading, MA, 1969), corrected, slightly enlarged edition reprinted by Dover Publications in 1990, 1990, p. 513.
[31] Conn, Gould, Toint, Trust-Region Methods, MPS-SIAM Series on Optimization, Series Number 1, 2000. https://doi.org/10.1137/1.9780898719857.
[32] Perier-Muzet, Stutz, Numerical study of the effectiveness of a vertical falling plate film absorber for an absorption chiller, Int. J. Refrig. 127 (2021) 221–229, https://doi.org/10.1016/j.ijrefrig.2021.02.013.
[33] A. Saul, W. Wagner, International Equations for the Saturation Properties of Ordinary Water Substance, J. Phys. Chem. Ref. Data 16 (4) (1987) 893–901, https://doi.org/10.1063/1.555787.
[34] G.A. Florides, S.A. Kalogirou, S.A. Tassou, L.C. Wrobel, Design and construction of a LiBr–water absorption machine, Energy Convers. Manage. 44 (15) (2003) 2483–2508, https://doi.org/10.1016/s0196-8904(03)00006-2.
[35] Q. Qiu, X. Zhang, S. Quan, X. Zhu, S. Shen, 3D numerical study of the liquid film distribution on the surface of a horizontal-tube falling-film evaporator, Int. J. Heat Mass Transf. 124 (2018) 943–952, https://doi.org/10.1016/j.ijheatmasstransfer.2018.04.020.